

Supporting Information:

Isolated Zirconium Centres Captured from Aqueous Solution: The Structure of Zirconium Mandelate Revealed from NMR Crystallography

James M. Crosland, Emily K. Corlett, Dave Scapens, Nathalie Guillou, Steven P. Brown and Richard I. Walton

S1: Laboratory characterisation Laboratory powder X-ray diffraction (PXRD) patterns spanning a 2θ range of $5 - 60^\circ$ were measured on a Siemens D5000 diffractometer (Bragg-Brentano geometry) operating with $\text{Cu K}\alpha_{1/2}$ with a step size of 0.05° , using a background-free silicon sample holder (Figs S1 and S2). Thermogravimetric analysis (TGA) of samples was carried out in open $70 \mu\text{l}$ alumina pans with a Mettler Toledo STARe TGA/DSC, with heating from room temperature to 1000°C at $10^\circ\text{C}/\text{min}$ under an air atmosphere (gas flow of $50 \text{ ml}/\text{min}$) (Fig. S3). Infrared spectra were taken using a Bruker Alpha FTIR spectrometer across a spectral range of $400 - 4000 \text{ cm}^{-1}$ as an average of 16 scans, each with a resolution of 2 cm^{-1} . Solid material was held against the diamond ATR cell with the instrument anvil. Pre-sample measurement background measurements were performed under the same conditions but with the anvil unused. Spectra were baseline corrected using the instrument software (Fig. S4). SEM images of solids were gathered using a Zeiss SUPRA 55-VP scanning electron microscope. An ultrasonically dispersed suspension of sample material in acetone was applied to a sample stub and allowed to dry before being carbon coated prior to imaging (Fig. S5).

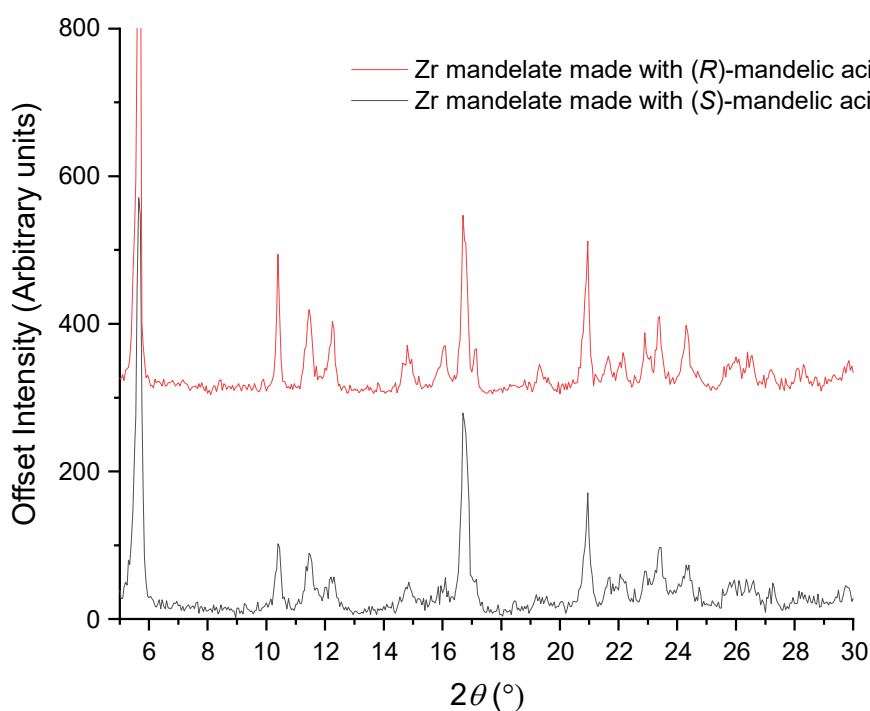


Figure S1 Laboratory PXRD patterns for zirconium mandelate made with (*R*)-mandelic acid only (top) and (*S*)-mandelic acid only (bottom), both in combination with zirconium sulfate.

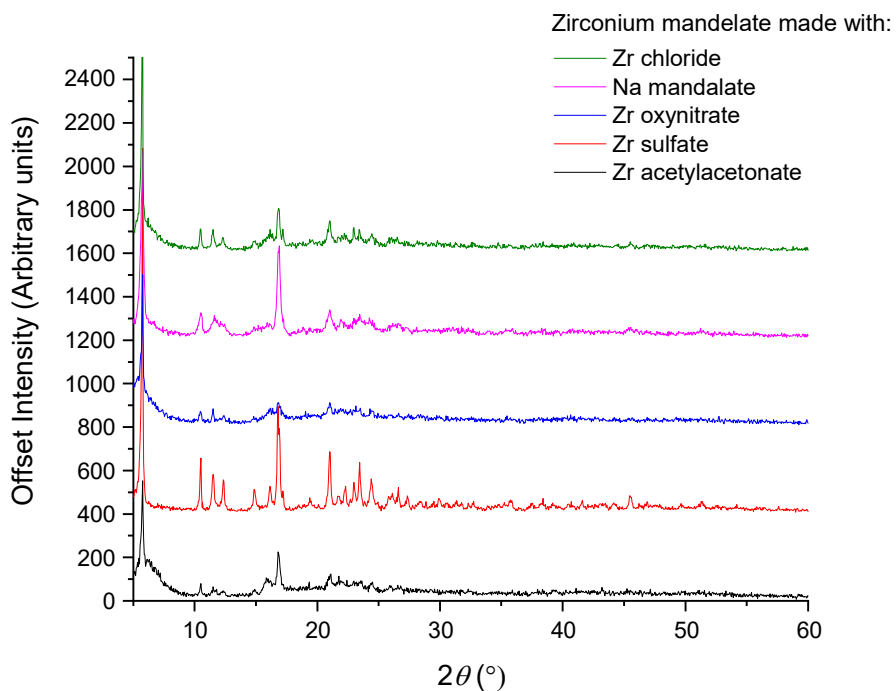


Figure S2 PXRD patterns for zirconium mandelate made with a variety of zirconium precursors, and with sodium mandelate.

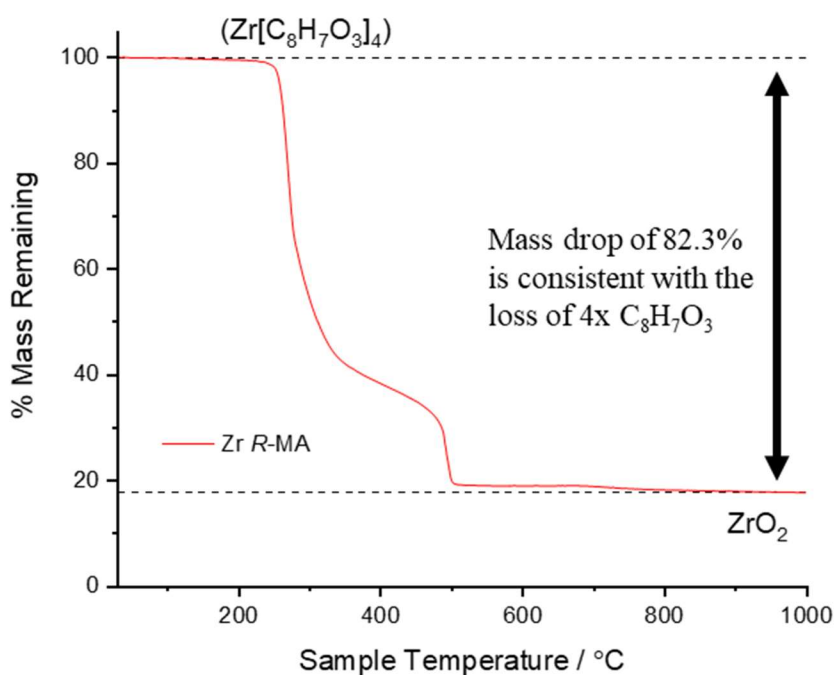


Figure S3 A plot of the mass loss during heating from the thermogravimetric analysis (TGA) of zirconium mandelate. The result here matches the expected mass loss to form ZrO₂ of 82.3%.

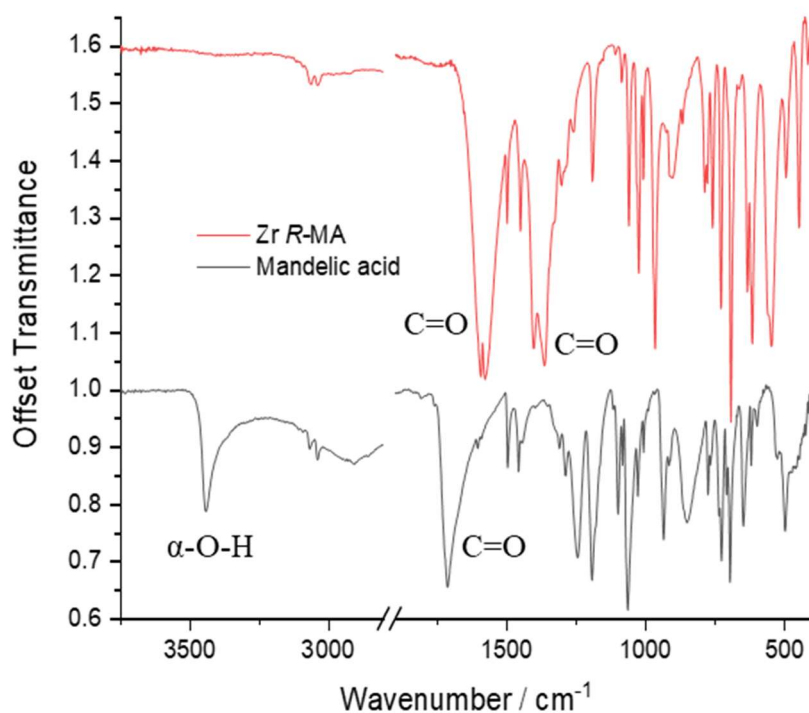


Figure S4 FTIR spectrum of zirconium mandelate made with (*R*)-mandelic acid (top) compared to the spectrum of free mandelic acid (bottom). Assignments of key bands are given.

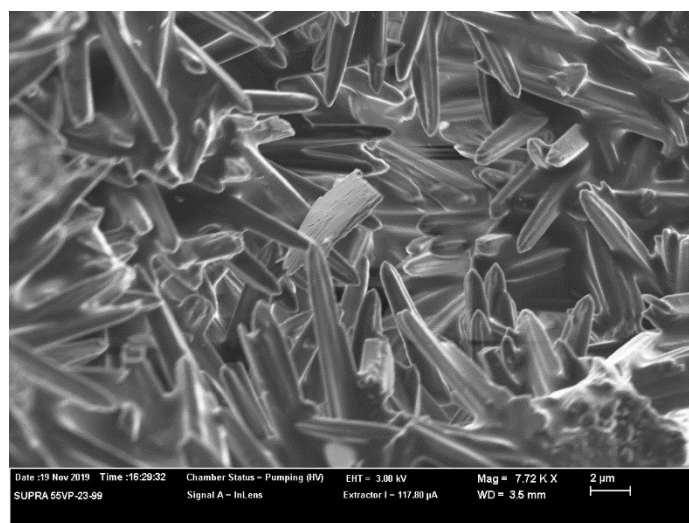


Figure S5 A scanning electron microscopy (SEM) image of zirconium mandelate material, showing the needle-like morphology of the individual crystals.

S2: High-resolution powder XRD High-resolution XRD data were measured on the I11 beamline at the Diamond Light Source synchrotron under ambient conditions. A finely-ground sample was mounted in a spinning quartz capillary, and data were collected across a range of 2 - 92° with a step size of 0.004°. The incident X-ray beam wavelength was 0.82445(2) Å. Extractions of the peak positions,

pattern indexing, charge flipping, simulated annealing processes and Rietveld refinements were carried out with the TOPAS V5 program,¹ while the EXPO package² using EXTRA for extracting integrated intensities and SIR97 for direct-method structure solutions was used to initialize the structural model. The LSI-indexing method based on the first 20 peaks converged unambiguously to a monoclinic unit cell ($a = 17.0775(7) \text{ \AA}$, $b = 5.63423(10) \text{ \AA}$, $c = 16.9860(4) \text{ \AA}$, $\beta = 114.885(3)^\circ$ & $V = 1482.62(8) \text{ \AA}^3$) with a satisfactory figure of merit ($M_{20} = 29$). A careful examination of the small peaks concluded that only extinctions compatible with a c glide plane were possible. Taking into account the chirality of the organic ligand, the non-centrosymmetric Pc space group was chosen to initialise the structural determination, and charge flipping and direct-methods simultaneously allowed the Zr localisation. The atomic coordinates of Zr were used as a starting model in the Rietveld refinement and the direct space strategy was then used to localise the four mandelate anions, which have been added and treated as rigid bodies in a simulated annealing process. The organic moieties were treated as rigid bodies and C-C distances refined. The first structure solution yielded a set of atomic-coordinates from which, by comparison of the GIPAW calculated and experimental NMR chemical shifts (see Section S4), the structure was adjusted to reach a structural model which agreed with both XRD and NMR. At the final stage, Rietveld refinement involved the following structural parameters: 1 atomic y coordinate for Zr, 24 parameters for the localization of the organic ligands, 4 mean C-C C-O distances, 8 torsion angles, 1 overall thermal factor and 1 scale factor for 1720 reflections. The anisotropic line broadening effect was modelled using the Stephens' model. Hydrogen atoms were placed by geometric constraint, with the H atoms of OH groups placed to counterbalance the charge but allowed to rotate freely. The final Rietveld plot corresponds to a satisfactory model indicator $R_B = 0.017$ and profile factors $R_p = 0.035$ and $R_{wp} = 0.049$. The above data analysis was aided by density measurement of the as-made material using helium pycnometry (1.17 g cm^{-3}), which suggested the number of zirconium centres in the unit cell to be two.

S3: EXAFS spectroscopy EXAFS measurements were carried out on the B18 Core XAS beamline³ at Diamond Light Source, at the zirconium K-edge (Fig. S6 & Table S1). Data were collected from samples diluted with appropriate amounts of polyethylene powder and pressed in self-supporting discs around 1 mm thick in transmission mode. Incident energies were selected using a water-cooled, fixed-exit, double-crystal monochromator with Si(311) crystals. The beam was focussed horizontally and vertically using a double toroidal mirror, coated with Pt, 25 m from the source, while a pair of smaller plane mirrors were used for harmonic rejection. The raw data were normalised using the software ATHENA⁴ to produce XANES spectra and EXAFS spectra for modelling using the software ARTEMIS.⁴ The k^2 -weighted Zr K-edge EXAFS spectra were analysed over the k -range 3 - 15.9 \AA^{-1} .

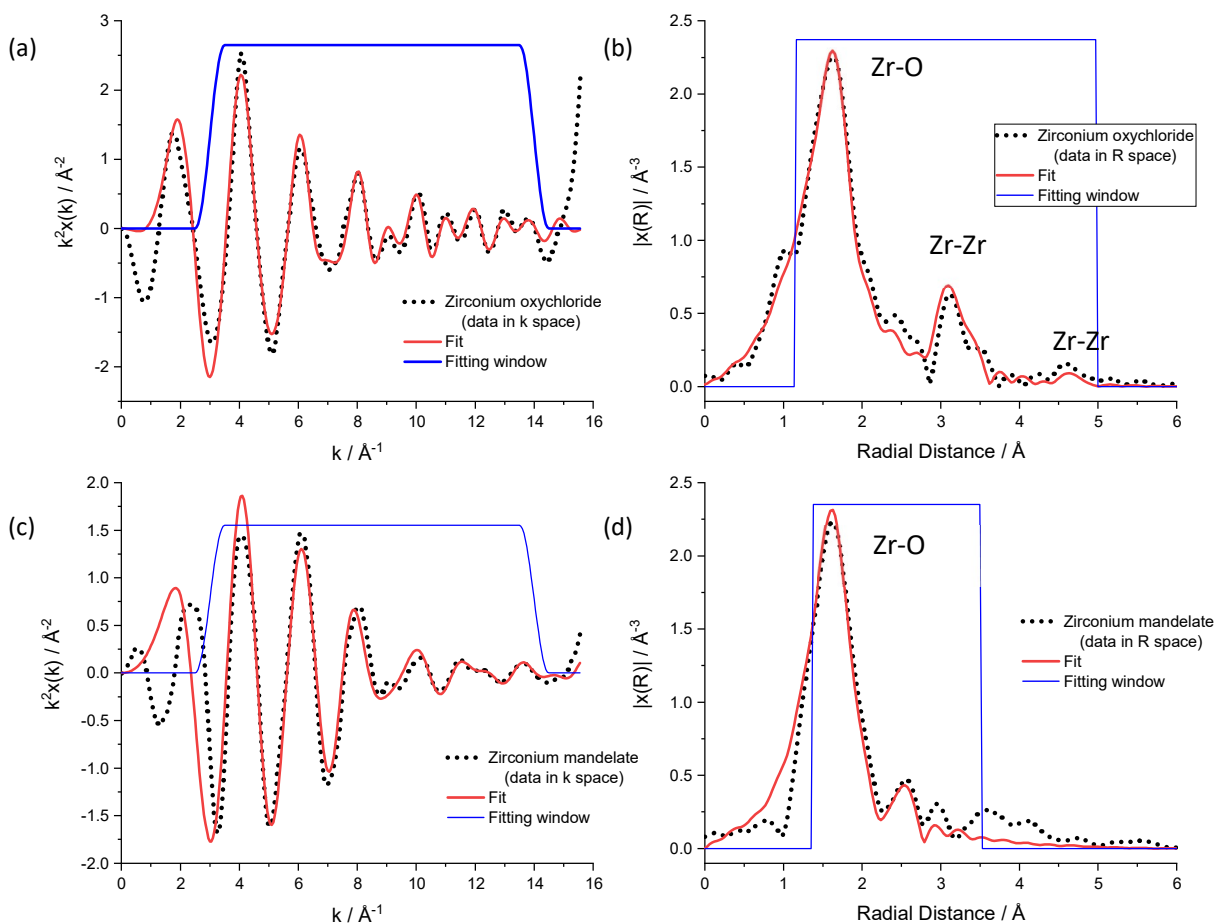


Figure S6 (a) Fit to EXAFS data in k -space for zirconium oxychloride; (b) corresponding fit and data in R -space for zirconium oxychloride. (c) Fit to EXAFS data in k -space for zirconium mandelate; (d) corresponding fit and data in R -space for zirconium mandelate. The crystal structure of zirconium oxychloride is known to contain the zirconium tetramer; as such contributions are seen in the R -space plot for the Zr-Zr square-edge and the Zr-Zr diagonal correlations at $\sim 3.2 \text{ \AA}$ & 4.6 \AA (plot values), respectively. Such features are absent from the results for zirconium mandelate, suggestive of isolated zirconium centres. Atomic correlations for Zr-O and Zr-Zr are labelled. Note that the interatomic distances presented in the R space plots are phase shifted from the true values by approximately 0.5 \AA .

Table S1: Refined EXAFS parameters from the data analysis in Figure S5. The atom label in the *Shell* column denotes a particular scattering path included in the overall fit (Zr to O/C). R_{eff} is the corresponding average interatomic distance as per the material's crystal structure; R is the refined distance adjusted during the fit. N , σ^2 , S_0^2 & E_0 represent coordination number, atomic position mean-squared disorder, amplitude reduction factor and threshold energy, respectively.

Zirconium oxychloride					Zirconium mandelate				
<i>Shell</i>	$R_{\text{eff}} / \text{\AA}$	N	$\sigma^2 / \text{\AA}^2$	$R / \text{\AA}$	<i>Shell</i>	$R_{\text{eff}} / \text{\AA}$	N	$\sigma^2 / \text{\AA}^2$	$R / \text{\AA}$
<i>O</i>	2.124	3	0.00462 ± 0.01292	2.136 ± 0.142	<i>O</i>	2.189	5	0.00347 ± 0.00186	2.127 ± 0.024
<i>O</i>	2.210	3	0.00462 ± 0.01292	2.205 ± 0.176	<i>O</i>	2.240	3	0.00209 ± 0.00278	2.255 ± 0.034
<i>O</i>	2.326	2	0.00381 ± 0.00237	2.233 ± 0.045	<i>C</i>	2.650	2	0.00116 ± 0.00591	2.683 ± 0.075
<i>Zr</i>	3.559	2	0.00505 ± 0.00089	3.573 ± 0.012	<i>C</i>	3.014	2	0.00116 ± 0.00964	3.035 ± 0.065
<i>Zr</i>	5.032	1	0.00810 ± 0.00667	5.038 ± 0.070	<i>C</i>	3.135	2	0.00247 ± 0.00964	2.829 ± 0.128
$S_0^2 = 1.682, E_0 = -5.047 \pm 2.298 \text{ eV}$					$S_0^2 = 1.682, E_0 = -7.396 \pm 4.089 \text{ eV}$				

S4: Solid-State NMR Solid-state NMR magic angle spinning (MAS) experiments were performed on a Bruker Avance II+ spectrometer, operating at ^1H and ^{13}C Larmor frequencies of 600.0 MHz and 150.7 MHz, respectively, using a 4 mm HX probe and a 1.3 mm HXY probe for ^1H - ^{13}C cross polarisation (CP) and ^1H one-pulse experiments. A ^1H 90° pulse length of 2.5 μs was used. SPINAL64⁵ ^1H heteronuclear decoupling was applied during the acquisition of the ^{13}C FID, with a pulse duration of 5.9 μs at a nutation frequency of 100 kHz, and a 70 to 100 % ramp⁶ on the ^1H channel was used for the CP contact time with nutation frequencies of 47.5 and 60 kHz for ^{13}C and ^1H , respectively.

Density functional theory (DFT) calculations were performed using CASTEP Academic Release version 16.1.⁷ All calculations used the Perdew Burke Ernzerhof (PBE) exchange correlation functional,⁸ a plane-wave basis set with ultrasoft pseudopotentials and a plane-wave cut-off energy of 700 eV. Integrals over the Brillouin zone were taken using a Monkhorst-Pack grid of minimum sample

spacing $0.08 \times 2\pi \text{ \AA}^{-1}$. Geometry optimisations were performed with unit cell parameters fixed but all atoms free to move. NMR parameters were calculated for the geometry optimised structure using the gauge-including projector-augmented wave (GIPAW) approach.⁹ The calculated isotropic chemical shifts ($\delta_{\text{iso}}^{\text{calc}}$) were determined from the calculated chemical shieldings (σ_{calc}) by $\delta_{\text{iso}}^{\text{calc}} = \sigma_{\text{ref}} - \sigma_{\text{calc}}$, with a σ_{ref} value of 169.0 ppm for ^{13}C . σ_{ref} was determined for ^{13}C by taking the sum of the experimental chemical shift and the GIPAW calculated absolute isotropic chemical shieldings. The resulting y-intercept was taken as σ_{ref} .^{10,11}

GIPAW calculations were performed for each subsequent structural model and the resulting chemical shifts compared to the experimental solid-state NMR. The agreement between experiment and GIPAW calculation for organic molecules has an established discrepancy of 1% of the chemical shift range (~ 2 ppm for ^{13}C).¹²⁻¹⁵ Initial structural solutions showed good agreement for all carbon environments except that of the hydroxyl carbon, for which the calculated ^{13}C chemical shifts for three of the mandelate molecules were more than 4 ppm higher (4.3-5.8 ppm) than the corresponding experimental resonances (Figure S7). It was also noted that overlap in the experimental resonances produced two peaks of equal height, suggesting that hydroxyl carbon resonances from two of the four mandelate molecules contributed to each, while the separation in GIPAW calculated chemical shifts would suggest a 3:1 ratio instead. This helped inform the generation of subsequent models, which were refined against the powder X-ray pattern until the ratio and chemical shift values from GIPAW calculation were in agreement with the experimental data.

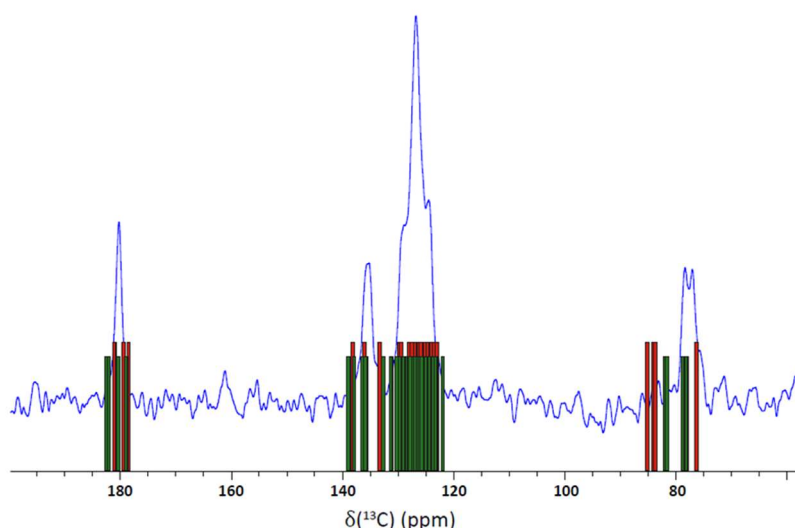


Figure S7 (a) Solid-state ^1H - ^{13}C CP MAS ($\nu_{\text{R}} = 12.5$ kHz) NMR spectra ($\nu_0(^1\text{H}) = 600$ MHz) of zirconium mandelate recorded with a contact time of 1.5 ms, 16 co-added transients for a recycle delay of 60 s. The experimental data (blue plots) are overlaid with GIPAW calculated chemical shifts for the initial (red bars) and final (green bars) structural models.

1. *Topas V5: General Profile and Structure Analysis Software for Powder Diffraction Data*, Bruker AXS Ltd, 2014.
2. A. Altomare, C. Cuocci, C. Giacovazzo, A. Moliterni, R. Rizzi, N. Corriero & A. Falcicchio, *J. Appl. Cryst.*, 2013, **46**, 1231-1235.
3. A. J. Dent, G. Cibin, S. Ramos, A. D. Smith, S. M. Scott, L. Varandas, M. R. Pearson, N. A. Krumpa, C. P. Jones and P. E. Robbins, *Phys. Conf. Ser.*, 2009, **190**, 012039.
4. B. Ravel and M. Newville, *J. Synchrotron Radiat.*, 2005, **12**, 537-541.
5. B. M. Fung, A. K. Khitrin & K. Ermolaev, *J. Magn. Reson.*, 2000, **142**, 97-101.
6. G. Metz, X. L. Wu & S. O. Smith, *J. Magn. Reson., Ser. A*, 1994, **110**, 219-227.
7. S. J. Clark, M. D. Segall, C. J. Pickard, P. J. Hasnip, M. J. Probert, K. Refson & M. C. Payne, *Z. Kristallogr.*, 2005, **220**, 567-570.
8. J. P. Perdew, K. Burke & M. Ernzerhof, *Phys. Rev. Lett.*, 1996, **77**, 3865-3868.
9. C. J. Pickard & F. Mauri, *Phys. Rev. B*, 2001, **63**, 245101.
10. G. N. M. Reddy, D. S. Cook, D. Iuga, R. I. Walton, A. Marsh & S. P. Brown, *Solid State Nucl. Magn. Reson.*, 2015, **65**, 41-48.
11. R. K. Harris, P. Hodgkinson, C. J. Pickard, J. R. Yates & V. Zorin, *Magn. Reson. Chem.*, 2007, **45**, S174-S186.
12. D. V. Dudenko, P. A. Williams, C. E. Hughes, O. N. Antzutkin, S. P. Velaga, S. P. Brown and K. D. M. Harris, *J. Phys. Chem. C*, 2013, **117**, 12258-12265.
13. R. K. Harris, P. Y. Ghi, H. Puschmann, D. C. Apperley, U. J. Griesser, R. B. Hammond, C. Y. Ma, K. J. Roberts, G. J. Pearce, J. R. Yates and C. J. Pickard, *Org. Proc. Res. Dev.*, 2005, **9**, 902-910.
14. J. R. Yates, S. E. Dobbins, C. J. Pickard, F. Mauri, P. Y. Ghi and R. K. Harris, *Phys. Chem. Chem. Phys.*, 2005, **7**, 1402-1407.
15. A. L. Webber, L. Emsley, R. M. Claramunt and S. P. Brown, *J. Phys. Chem. A*, 2010, **114**, 10435-10442.